

Article

Rotational Energy Extraction from the Kerr Black Hole's Mimickers

Vishva Patel ¹ , Kaunthey Acharya ¹, Parth Bambhaniya ^{1,*}  and Pankaj S. Joshi ^{1,2}¹ International Center for Cosmology, Charusat University, Anand 388421, Gujarat, India² International Centre for Space and Cosmology, Ahmedabad University, Ahmedabad 380009, Gujarat, India

* Correspondence: grcollapse@gmail.com

Abstract: In this paper, the Penrose process is used to extract rotational energy from regular black holes. Initially, we consider the rotating Simpson–Visser regular spacetime, which describes the class of geometries of Kerr black hole mimickers. The Penrose process is then studied through conformally transformed rotating singular and regular black hole solutions. Both the Simpson–Visser and conformally transformed geometries depend on mass, spin, and an additional regularisation parameter l . In both cases, we investigate how the spin and regularisation parameter l affect the configuration of an ergoregion and event horizons. Surprisingly, we find that the energy extraction efficiency from the event horizon surface is not dependent on the regularisation parameter l in the Simpson–Visser regular spacetimes, and hence, it does not vary from that of the Kerr black hole. Meanwhile, in conformally transformed singular and regular black holes, we obtain that the efficiency rate of extracted energies is extremely high compared to that of the Kerr black hole. This distinct signature of conformally transformed singular and regular black holes is useful to distinguish them from Kerr black holes in observation.

Keywords: Penrose process; regular black holes; energy extraction



Citation: Patel, V.; Acharya, K.; Bambhaniya, P.; Joshi, P.S. Rotational Energy Extraction from the Kerr Black Hole's Mimickers. *Universe* **2022**, *8*, 571. <https://doi.org/10.3390/universe8110571>

Academic Editors: Sergei B. Popov and Ziri Younsi

Received: 9 September 2022

Accepted: 26 October 2022

Published: 30 October 2022

Publisher's Note: MDPI stays neutral with regard to jurisdictional claims in published maps and institutional affiliations.



Copyright: © 2022 by the authors. Licensee MDPI, Basel, Switzerland. This article is an open access article distributed under the terms and conditions of the Creative Commons Attribution (CC BY) license (<https://creativecommons.org/licenses/by/4.0/>).

1. Introduction

The way mankind has witnessed a series of scientific breakthroughs in astrophysics, including the detection of gravitational waves from the merger of two black holes, the shadow images of M87*, and the Milky way galactic centre Sgr- A* [1–8], has drawn the attention of not just the scientific community but also the general public. These observations by the EHT group have opened the way for gravitational theories to be verified in strong gravity regimes. The EHT group's findings have been used to constrain and study various aspects of gravity theories, extending from general relativity to its alternatives.

Stars having more mass than about 10 solar masses collapse under their own gravity at the end of their lives since they cannot balance their gravitational pull by any known quantum pressures. Thus, according to Einstein's general theory of relativity, the continuous gravitational collapse of a massive star culminates in a spacetime singularity that contains infinite matter density and gravitational field. At this point, all physical quantities diverge and become arbitrarily large. This ultra-dense region can be anticipated by modelling various astrophysical compact objects, such as black holes, naked singularities, worm holes, and other specific types of these objects. These compact objects, together with gravitational waves and shadows, are considered one of the most efficient sources of energy in the universe. As a result, they are assumed to be responsible for a gigantic electromagnetic environment in their near vicinity, as well as high-energy jet emission outbursts that destroy nearby stars and galaxies.

In various literature, researchers have explored the different observational properties of different possible compact objects (black holes, naked singularities, and wormholes) for, e.g., the shadow properties, [9–21], gravitational lensing [22–28], accretion disk properties [29–36], and orbital precession [37–45]. Similar observable properties were studied in

singularity-free compact objects (regular black holes and worm holes) [46–57]. The major problem of powering active galactic nuclei, X-ray binaries, and quasars are the most important issues today in high-energy astrophysics. Several mechanisms have been proposed by various authors in different scenarios to explain these high-energy phenomena [58,59].

In 1969, Roger Penrose presented an innovative and novel approach to extract energy from a rotating black hole. The Penrose process is dependent on the existence of an ergosphere, which is described as the region between an event horizon and the static surface limit. Since Penrose and Floyd [60] did not mention astrophysical implications of the Penrose process, Wheeler [61] and others stated that the process could offer a reasonable solution for high-energy jets coming from active galactic nuclei. This mechanism is known for having a star-like object approach a supermassive compact object and afterward break up into fragments due to immense tidal forces. Some fragments may have negative energy orbits, while others escape at extremely high velocity, generating a jet. As a consequence, the Penrose process has been reintroduced as a mechanism for high-energy sources. After a thorough investigation, multiple approaches (super-Penrose process, collisional process, BSW (Banados–Silk–West) effect) for various scenarios have been proposed [62–68]. In [69–73]. Authors have studied the super-Penrose process with charged particles with near-naked singularities, white holes, and wormholes. Researchers have also studied energy extraction in different scenarios such as extremal rotating electrovacuum black holes using particle collision [73–79] and the Penrose process in axially symmetric magnetized black holes [80].

As we all know, one of the fundamental problems in physics is the emergence of a curvature singularity within the general theory of relativity. Under certain physically reasonable conditions, these phenomena reflect regions where geodesics abruptly terminate, and their occurrence is usually interpreted as indicating the theory’s breakdown. It is generally speculated that quantum gravitational effects will prevent singularities from forming as an end state of gravitational collapse. However, a reasonable interpretation of such small-scale effects remains unclear. There have been various attempts to overcome the occurrence of singularities [81–93]. Motivated by this, in this paper, we consider singularity-free solutions to study the Penrose process.

Initially, we consider a family of spacetime geometries proposed by Simpson and Visser [94,95] that contains a class of solutions (one-way wormhole, two-way wormhole, and regular black hole) depending on the regularisation parameter l , which is the exact solution to the Einstein field equations [96]. Then, we consider the conformally transformed solutions presented in [97], where singularity-free black hole solutions have been proposed within a broad class of conformally invariant gravity theories. The authors propose singular and regular black hole solutions. These conformally transformed black hole spacetimes are a solution of conformal vacuum Einstein field equations (CEFE). For a regular black hole solution at $r = 0$, the curvature invariants do not diverge, demonstrating that the proposed spacetimes are geodesically complete [98]. The action in a conformally invariant theory of gravity is invariant under both generalized and conformal coordinate transformations.

As mentioned above, the observational properties have been studied in various research for different non-singular compact objects. Moreover, the phenomenology of energy extraction has been studied in many cases where the compact objects could have horizons and a central singularity. It is, therefore, worth studying the energy extraction from non-singular compact objects. Therefore, in this paper, we consider the conformal rotating singular and non-singular spacetimes along with regular Simpson–Visser metrics, which we use to study the phenomenology of the Penrose process.

This paper is assembled as follows. In Section 2, we obtain the general formalism of the Penrose process. In Section 3, we discuss the energy extraction rate from Simpson–Visser spacetimes. In Section 4, we discuss the singular and regular black hole solutions and compare the efficiency of extracted energies with that of Kerr black holes. Finally, in Section 5, we wrap up the study and discuss the results. Throughout the paper, we

consider geometrized units. Thus, the gravitational constant (G) and the speed of light (c) are set equal to one. The signature of the metric is considered to be $(-,+,+,+)$.

2. The Penrose Process for Energy Extraction from a Rotating Black Hole

The Penrose process, which allows us to extract rotational energy from black holes, is discussed in this section. Rotational energy extraction requires the presence of an ergoregion, which refers to the region between an event horizon and the static limit surface (SLS). There are considerable examples in which a rotating spacetime forms an ergoregion without an event horizon [99]. However, in this work, we consider spacetime in which the horizon is present without a spacetime singularity. The Penrose process is well-known, which is why we give only a quick overview of it.

In order to understand this process, let us assume an incident particle (0) splits into two particles ((1) and (2)) in the ergoregion. One of them, (1), crosses the event horizon while the other one, (2), escapes to infinity. As a consequence, the escaping one (2) might have energy higher than the original (0) test particle. Assume particle (0) falling into an ergoregion has energy $E_{(0)} \geq 1$. As the particle is separated into two fragments in the ergoregion, the energy is $E_{(1)}$ and $E_{(2)}$. As mentioned above, particle (2) escapes to infinity with energy $E_{(2)} > 0$, whereas the other one falls into the black hole with negative energy $E_{(1)} < 0$. Taking this into consideration, the particle follows the conservation laws for different parameters in the ergosphere, which can be written as:

$$E_{(0)} = E_{(1)} + E_{(2)}, \quad L_{(0)} = L_{(1)} + L_{(2)},$$

$$M_{(0)} = M_{(1)} + M_{(2)}.$$

According to the formalism of the Penrose process, the condition $E_{(1)} < 0$ should be fulfilled. In order to figure out how efficient energy extraction is, we consider a very simple scenario in which the test particles are restricted on an equatorial ($\theta = \pi/2$) plane; thus, the conserved momentum is:

$$P_{(0)}^\mu = P_{(1)}^\mu + P_{(2)}^\mu.$$

The momenta of three particles P_j^μ ($j = 0, 1, 2$) are non-spacelike, and therefore they should lie inside the local light cone. The orbit of a particle moving on a plane is described by two-dimensional coordinates: radial and angular coordinates (r and ϕ). Then, we can write the momentum of a particle along the geodesic γ as

$$P_\gamma = P^t \left(\frac{\partial}{\partial t} + v \frac{\partial}{\partial r} + \Omega \frac{\partial}{\partial \phi} \right), \tag{1}$$

where $v = dr/dt$ and $\Omega = d\phi/dt$. The conserved energy relation is defined as $E = -P_t$, and it gives

$$P^t = -\frac{E}{X}, \tag{2}$$

$$X = g_{tt} + \Omega g_{t\phi}. \tag{3}$$

Now, from $P^\mu P_\mu = -M^2$, we get an expression of the geodesic motion as

$$g_{tt} + v^2 g_{rr} + 2\Omega g_{t\phi} + \Omega^2 g_{\phi\phi} = -\left(\frac{MX}{E}\right)^2. \tag{4}$$

As we have mentioned, particle (1), which crosses the horizon, will have negative energy, i.e., $E_{(1)} < 0$, whereas the second particle (2) will escape to infinity as it gets rotational energy by the Penrose process. Therefore, the efficiency of energy extraction in the Penrose process is defined as

$$\eta = \frac{E_{(2)}}{E_{(0)}} - 1. \tag{5}$$

From the conserved energy and angular momentum, one can redefine the energy and angular velocity as

$$\frac{E_{(2)}}{E_{(0)}} = \frac{(\Omega_{(0)} - \Omega_{(1)})X_{(2)}}{(\Omega_{(2)} - \Omega_{(1)})X_{(0)}}. \tag{6}$$

Note that here we consider the case in which an incident particle has $E_{(0)} = M_{(0)}$ and assume that it will decay into two fragments with momentum $P_{(1)}$ and $P_{(2)}$. Now, from Equation (6), one can see that the efficiency η is maximized when we consider the largest value of $\Omega_{(2)}$ and the smallest value of $\Omega_{(1)}$. We can get maximum efficiency when the term dr/dt vanishes in Equation (1) for both particles. So ultimately, we can obtain the general expression of the efficiency rate for the maximum extracted energy as

$$\eta_{max} \leq \frac{g_{\phi\phi}(\sqrt{1 + g_{tt}} + 1) + g_{t\phi}^2}{2g_{\phi\phi}\sqrt{1 + g_{tt}}} - 1. \tag{7}$$

The maximum energy can be extracted if we consider the fragment splitting at the outer horizon, and the same scenario is given for the Penrose process. In expression (7), an equality shows that the splitting of a particle is happening at the outer horizon. Now, if we use the metric tensor components of the Kerr black hole in Equation (7), then we can get that the maximum efficiency of extracted energy for extreme spin parameter ($a = M$) is 20.7%. Let us move to the next section in which we look for rotating Simpson–Visser spacetime for the same scenario.

3. Rotating Simpson–Visser Spacetime

In [100], Simpson and Visser proposed a spherically symmetric spacetime that smoothly interpolates between a Schwarzschild black hole ($l = 0$) and Morris–Thorne wormholes with regular geometry. However, the more physical scenario can be considered by introducing the spin parameter (a) in this metric. The rotating Simpson–Visser spacetime is derived using the Janis–Newmann algorithm in [94,95]. The metric for that spacetime can be written as

$$ds^2 = -\left(1 - \frac{2M\sqrt{r^2 + l^2}}{A}\right)dt^2 + \frac{A}{\Delta}dr^2 + Ad\theta^2 - \frac{4Ma\sqrt{r^2 + l^2}\sin^2\theta}{A}dtd\phi + \left(r^2 + a^2 + l^2 + \frac{2Ma^2\sqrt{r^2 + l^2}\sin^2\theta}{A}\right)\sin^2\theta d\phi^2, \tag{8}$$

where

$$A = r^2 + l^2 + a^2\cos^2\theta, \quad \Delta = r^2 + l^2 + a^2 - 2M\sqrt{r^2 + l^2}.$$

Here, M denotes the ADM mass of the spacetime metric, and l is a regularisation parameter. The metric given in (8) reduces to the Kerr spacetime with $l = 0$ and a Schwarzschild spacetime with vanishing spin (a) and regularisation (l) parameters. The rotating Simpson–Visser spacetime also possesses an inner horizon and an outer horizon, as well as an ergoregion. Inner and outer horizons are known as the Cauchy horizon and an event horizon, respectively. Depending on the different values of spin parameter a and regularisation parameter l , the nature of the compact object changes. One can understand how these properties of the compact object change by understanding how horizons and ergoregions are defined from the metric. For any general spacetime metric, the horizon can be defined by $g_{rr} = 0$. Thus, for the rotating Simpson–Visser metric, one can write the expression of the horizon radius as

$$r_{\pm} = \left(\left(M \pm \sqrt{M^2 - a^2}\right)^2 - l^2\right)^{\frac{1}{2}}, \tag{9}$$

where r_+ and r_- corresponds to outer and inner horizons, respectively.

Since we have considered a rotating black hole, the spacetime region around the centre of the compact object also possesses rotational motion. This is known as the frame-dragging effect. In the spacetime region up to a certain radius, the frame-dragging effect is so prominent that all particles also rotate with the rotating spacetime region around the compact object. The spacetime region where this effect is observed is known as an ergoregion. An observer can never be stationary in this region. Depending on the values of the different parameters in the spacetime metric components, the ergoregion changes. To study the change in the ergoregion, we need to know the mathematical expression of the ergoregion. For any general spacetime metric, the ergoregion can be defined by $g_{tt} = 0$. From this, the radius of the ergosphere in rotating Simpson–Visser can be expressed as

$$r_{erg\pm}^2 = \left(M \pm \sqrt{M^2 - a^2 \cos^2 \theta} \right)^2 - l^2. \tag{10}$$

Rotating Simpson–Visser spacetime suggests a regular geometry, as l is always positive ($l \neq 0$). Thus, a singularity would not exist for the rotating Simpson–Visser even at $r = 0$, and the metric represents a finitely sized surface with regular geometry.

From Equations (9) and (10), one can see that the mathematical expressions of these equations would be imaginary for certain values of a , M , and l . Thus, depending on different values of these quantities, physical properties of horizons and the ergoregion change, and thus, the nature of the compact object also changes. For these equations, their expressions are mathematically real and are thus physical only when $a < M$. For $a > M$, horizons would not exist, as the expressions of Equations (9) and (10) become imaginary. Such a geometry represents a wormhole, while for $a < M$, the shape of the ergoregion and the existence of horizons depend on the regularisation parameter l . If the regularisation parameter l is less than $M + \sqrt{M^2 - a^2}$ in Equation (9), then the event horizon exists, while for existence of the Cauchy horizon, the condition $l < M - \sqrt{M^2 - a^2}$ needs to be fulfilled. In such cases, the compact object would have both a Cauchy horizon and an event horizon with an ergoregion around them. That kind of geometry is known as a Regular Black Hole-2. However, for $a < M$, if the condition $l < M + \sqrt{M^2 - a^2}$ is satisfied, but the value of regularisation parameter l is larger than $M - \sqrt{M^2 - a^2}$, then only an event horizon would exist, as the expression of r_- becomes imaginary in Equation (9). This type of compact object is known as Regular Black Hole-1. However, for $l > M + \sqrt{M^2 - a^2}$, the geometry would not possess any horizon, and thus, it cannot be termed as regular black hole geometry. The different geometries of rotating Simpson–Visser spacetime related to different values of spin parameter and regularisation parameter is consistent with [101].

Until now, we have discussed cases for which $a < M$. However, compact objects have interesting geometrical features when $a = M$, because in this condition, for $l < M$, Equation (9) has the same mathematical expression for Cauchy horizon radius r_- and event horizon radius r_+ . Thus, both horizons would exist at just one particular radius. This compact object is termed an extremal regular black hole with degenerate horizons. Meanwhile, for $a = M$ and $l > M$, the geometry would not possess any horizon, as the expression in Equation (9) becomes imaginary, and thus, the compact object is not a black hole but rather a wormhole. One should note that as the spin parameter a is increased, the area of the ergoregion also increases, as one can see in Figure 1.

For the given rotating Simpson–Visser metric, we have shown different shapes of ergoregions corresponding to different values of a and l in (Figure 1). Starting with the low spin parameter $a = 0.1$, we get a Regular Black Hole-2 with both inner and outer horizons for a value of the regularisation parameter $l = 0.005$, which is less than $0.5 - \sqrt{0.5^2 - 0.1^2}$, as shown in Figure 1a. Meanwhile for a value of the regularisation parameter $0.5 - \sqrt{0.5^2 - 0.1^2} < l < 0.5 + \sqrt{0.5^2 - 0.1^2}$, there exists just an event horizon with Regular Black Hole-1 geometry, as one can see in Figure 1b. Finally, when $l > M + \sqrt{M^2 - a^2}$, expressions of both the event horizon and the Cauchy horizon become imaginary, as in Figure 1c. In a similar pattern, we show plots for different values of l

corresponding to compact objects with different physical and geometrical properties as we increase the value of spin parameter a while keeping the mass of the compact object $M = 0.5$. We get similar plots until we increase the spin parameter up to $a < M$, as one can see in Figure 1. One should note that as spin parameter a increase, the ergoregion also becomes larger, which can be seen in Figure 1.

However, when we change the spin parameter to $a = 0.5$, which is similar to the value of the mass of the compact object $M = 0.5$, we get different scenarios for different values of l . For $a = 0.5$, when $l < a$, the Cauchy horizon radius r_- and the event horizon radius r_+ have the same value. An extremal black hole representing this geometry with degenerate horizons can be seen in Figure 1j. Meanwhile for the same spin parameter $a = 0.5$, if the value of the regularisation parameter l is larger than the value of the spin parameter $a = 0.5$, then the compact object does not possess any horizon, as the expression of the horizon in Equation (9) again becomes imaginary, and the object is a wormhole, as one can see in Figure 1k. Now, finally considering the case where the spin parameter is taken to be $a = 0.6$, which is larger than $M = 0.5$, the expression of the Cauchy horizon, event horizon, and ergoregion becomes imaginary, which can be seen in Figure 1l. This geometry, again, represents a wormhole. One can go into the details of these different geometries, especially the nature of the throat of the wormholes for different values of regularisation parameter l and spin parameter a by studying their corresponding Penrose diagrams given in [95].

Energy Extraction by Penrose Process from Rotating Simpson–Visser Spacetime

As mentioned earlier, the extraction of energy by the Penrose process from the rotating object and the existence of the ergoregion and horizon are important. In the previous section, we discussed how ergoregions and horizons change with different values of the spin parameter and the regularisation parameter. It is evident that the expressions of horizons and ergoregions are different from those of a Kerr black hole, as one can see in Equations (9) and (10). As a consequence, energy extraction efficiency should differ from that of Kerr black holes. To check the energy extraction efficiency in the rotating Simpson–Visser spacetime, the angular velocity for an asymptotic observer at infinity can be derived. This shows the angular velocity for an asymptotic observer that resides on an equatorial plane. The maximum change on an ergoregion due to rotation can be observed at $\theta = \pi/2$. Therefore, the maximum energy efficiency that can be extracted from rotating Simpson–Visser spacetime is derived using (7)

$$\eta_{max} = \frac{1}{4} \left(\frac{2\sqrt{2}a^2M}{\left(\sqrt{\frac{M}{\sqrt{2M(\sqrt{M^2-a^2}+M)}-a^2}}\right) f_1(M, a)} + h_1(M, a) - 2 \right) 100, \quad (11)$$

where $f_1(M, a)$ and $h_1(M, a)$ are

$$f_1(M, a) = \left(a^2 \left(-\sqrt{M^2 - a^2} + \sqrt{2M(\sqrt{M^2 - a^2} + M) - a^2 - 3M} \right) + 4M^2(\sqrt{M^2 - a^2} + M) \right), \quad (12)$$

$$h_1(M, a) = \frac{\sqrt{2}}{\sqrt{\frac{M}{\sqrt{2M(\sqrt{M^2-a^2}+M)}-a^2}}}. \quad (13)$$

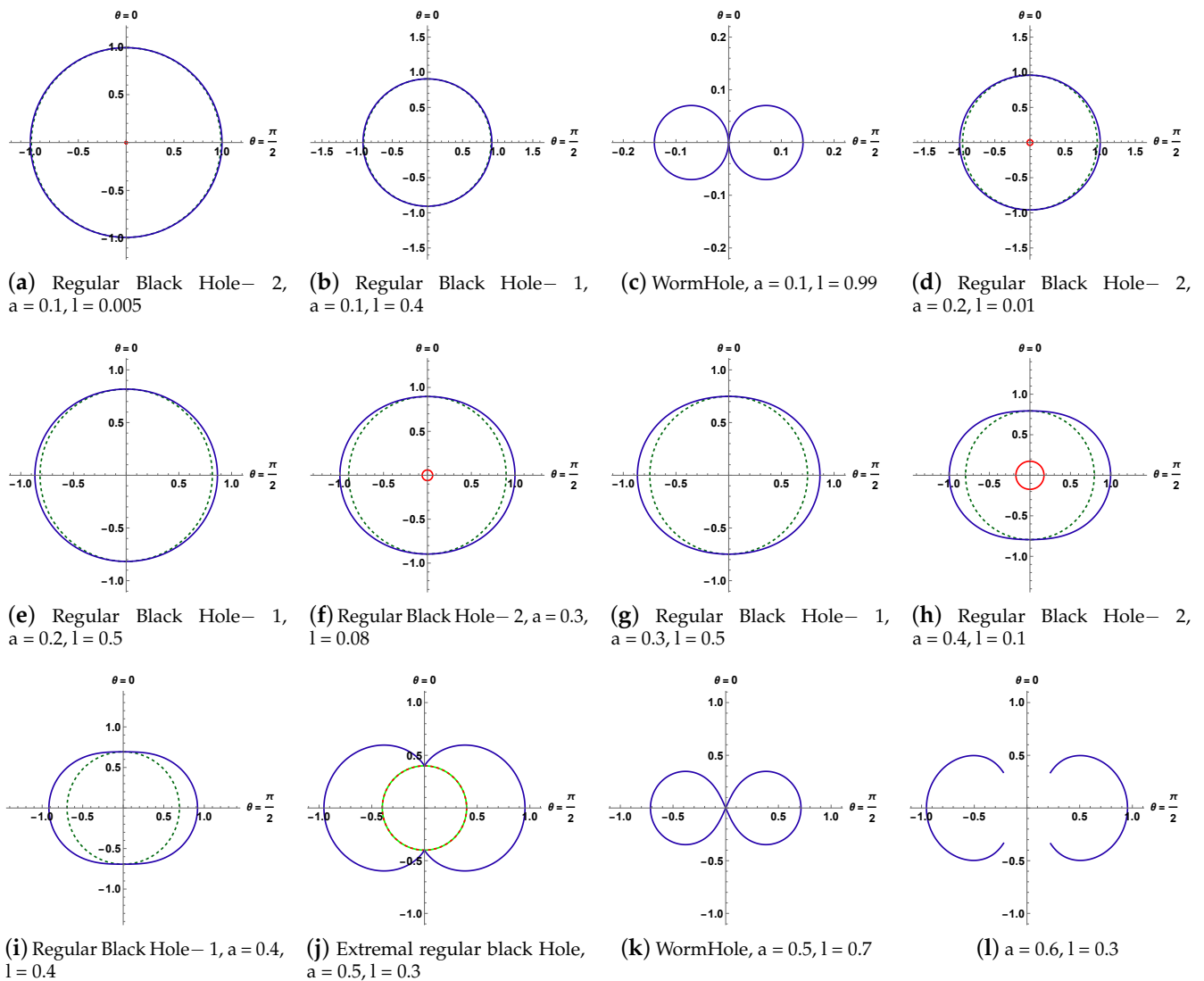


Figure 1. Figures show the behaviour of ergoregion and inner/outer horizon in rotating Simpson–Visser spacetime with different spin and regularisation parameters. The blue circle represents the boundary of the ergoregion, the green dotted circle represents the event horizon, and the red line represents the inner horizon; $M = 0.5$.

Surprisingly, it can be seen in the above expression that the energy efficiency depends only on the spin parameter a and not on the regularisation parameter l . The possible explanation for why energy extraction efficiency is independent of the regularisation parameter is mentioned in Section 5.

As the spin increases, the angular velocity increases, and energy extraction efficiency also increases. For $l = 0$, we get the energy efficiency for the Kerr metric. With the constant spin parameter, energy efficiency is the same for different values of the regularisation parameter l , as the energy efficiency does not depend on it. Thus, for regular black holes, energy extraction by the Penrose process is not possible in rotating Simpson–Visser spacetime, as the horizon does not exist in certain conditions, as discussed previously. As discussed in Section 2, it is also important to point out that energy extraction for the Penrose process is defined for the case in which particle splitting occurs at the event horizon, as we get the maximum efficiency in that condition. Thus, for the rotating Simpson–Visser metric also, the Penrose process is considered to be taking place at the event horizon only in this paper. As we move away from the event horizon, the energy efficiency decreases gradually in

the ergoregion, and outside the ergoregion, energy extraction efficiency drops significantly. Thus, we have defined the Penrose process for rotating Simpson–Visser spacetime, a class of regular compact objects where singularity is absent. In the next section, we discuss energy extraction in conformally transformed spacetimes.

4. Regular and Singular Black Hole Spacetimes

In [97], a conformally transformed rotating black hole solution is proposed. As aforementioned, these conformally transformed black hole spacetimes are the solution of CEFÉ. In Boyer–Lindquist coordinates, the metric can be written as,

$$dS^2 = S ds_{Kerr}^2, \tag{14}$$

where

$$S = \left(1 + \frac{l^2}{\Sigma}\right)^\nu, \tag{15}$$

$$\Sigma = r^2 + a^2 \cos^2 \theta,$$

where ν will determine whether the spacetime will represent regular or singular geometry. The values of ν for regular and singular black holes are 4 and 3, respectively, where $l > 0$ is a new parameter with a dimension of a length. The theory does not specify the value of l , although it is reasonable to assume that it is of the Planck length scale order, $l \approx P_l$, or of the order of the black hole mass, $l \approx M$, as these are the only two scales that are already in the model. In this paper, we consider the second scenario with l of the order of M because it is the only one with observational implications for astrophysical black holes. The line element of the Kerr black hole can be written as

$$ds_{Kerr}^2 = -\left(1 - \frac{2Mr}{\Sigma}\right) dt^2 - \frac{4Mar}{\Sigma} \sin^2 \theta dt d\phi + \frac{\Sigma}{\Delta} dr^2 + \Sigma d\theta^2 + \left(a^2 + r^2 + \frac{2Mra^2 \sin^2 \theta}{\Sigma}\right) \sin^2 \theta d\phi^2, \tag{16}$$

where $\Delta = r^2 - 2Mr + a^2$. The coordinate singularity in both spacetimes can be defined using $\Delta = 0$,

$$r_{\pm} = \left(M \pm \sqrt{M^2 - a^2}\right), \tag{17}$$

where r_{\pm} refers to outer and inner horizons. The ergoregion in both spacetimes can be determine using $g_{tt} = 0$,

$$r_{erg\pm} = \sqrt{M^2 - a^2 \cos^2(\theta)} + M. \tag{18}$$

One may note that the expressions for outer/inner horizons and the ergoregion are the same as in Kerr black holes. We use Equation (7) to determine the extracted energy efficiency rate in regular and a singular geometries. Here, in both black hole cases, the ergoregion is the same as what we have in the Kerr black hole, which one can understand from the mathematical expression defining that region. The ergoregion shows significantly evident changes for the cases $a > M$ and $a < M$. However, we consider only the case where $a < M$ for which the ergoregion exists. The changing of outer/inner horizons and ergoregion from $\theta = \pi/2$ to $\theta = 0$ with different spin parameters are shown in Figure 2. At $\theta = 0$, a spin effect of the object is the same as that of the Schwarzschild black hole, where the boundary of the ergoregion coincides with the horizons. On the other hand, the maximum effect of objects' spin can be perceived at $\theta = \pi/2$. All of this can be visualized in Figure 2. For extreme spin (where mass and spin are equal), the Cauchy and event horizons coincide, which can be seen in Figure 2a. The radius of the inner horizon decreases as object spin decreases. Moreover, as opposed to that, the radius of the outer horizon increases with decreasing object spin. The shape of an ergoregion also changes as the radius of the inner/outer horizons changes with the spin parameter (note that this is for slow rotation,

where the spin parameter is half of the mass). As the size of the ergoregion changes, the efficiency of energy extraction changes.

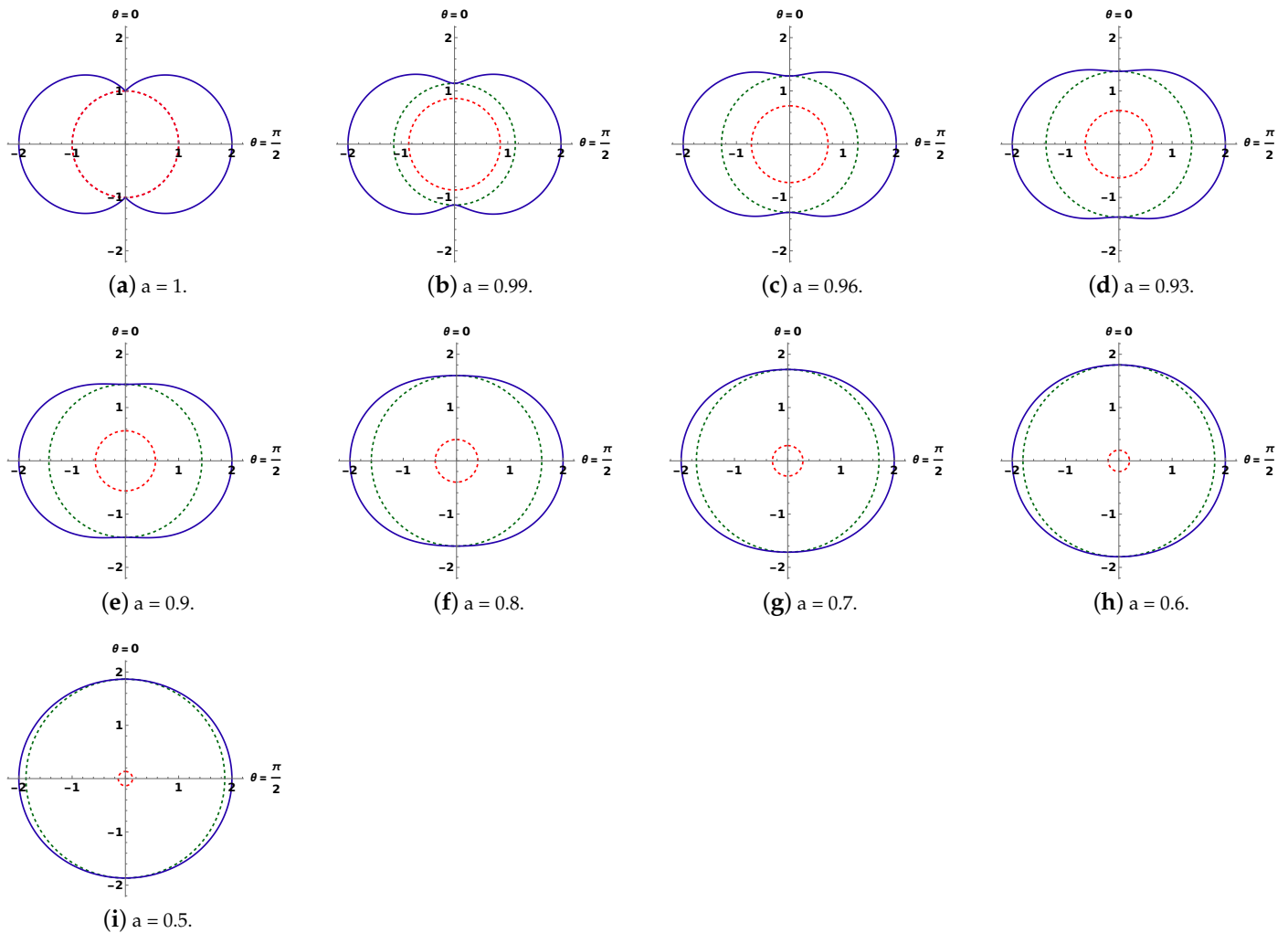


Figure 2. Behaviour of ergoregion and event horizon in regular and singular black hole spacetime with different parameters. The blue circle is for the outer boundary of the ergoregion, and the dotted green and red circles represent the outer and inner horizons, respectively. The mass is set equal to one for all the different parameters.

4.1. A Regular Black Hole

Let us first look at the regular black hole solution in (14), which can be obtained from the Kerr metric after using the rescaling factor (15). The line element for a regular black hole is written as

$$ds_{reg}^2 = \left(1 + \frac{l^2}{\Sigma}\right)^4 \left(-\left(1 - \frac{2Mr}{\Sigma}\right)dt^2 - \frac{4Mar}{\Sigma} \sin^2\theta dt d\phi + \frac{\Sigma}{\Delta} dr^2 + \Sigma d\theta^2 + \left(a^2 + r^2 + \frac{2Mra^2 \sin^2\theta}{\Sigma}\right) \sin^2\theta d\phi^2\right), \quad (19)$$

where ‘reg’ refers to the regular black hole. Using the Kretschmann scalar, one may get to know about the existence of a spacetime singularity. The Kretschmann scalar can be represented with the parameters of the Riemann curvature tensor as

$$K = R_{abcd} R^{abcd}, \quad (20)$$

For regular black hole spacetime, the Kretschmann scalar has the form

$$K = \frac{1}{(\Sigma + l^2)^n} (\text{Polynomial}, r, \cos\theta, M, a, l), \tag{21}$$

where n represents the integer number. This expression for the Kretschmann scalar is everywhere regular for $l \neq 0$, which means that K never diverges. When $l = 0$, we revive the well-known Kerr metric with the fact that the Kretschmann scalar diverges at $r \rightarrow 0$ with $\theta = \pi/2$.

The maximum energy extraction efficiency (when splitting happens at the event horizon) that can be extracted from the regular black hole is explored using Equation (7) with $\theta = \pi/2$:

$$\eta_{max(reg)} = \left(\frac{2a^2M^2(l^2 + r^2)^4}{r^9(a^2(2M + r) + r^3)\sqrt{1 - \frac{(l^2+r^2)^4(r-2M)}{r^9}}} + \frac{\sqrt{1 - \frac{(l^2+r^2)^4(r-2M)}{r^9}} + 1}{2\sqrt{1 - \frac{(l^2+r^2)^4(r-2M)}{r^9}}} - 1 \right) 100. \tag{22}$$

Table 1 represents the energy extraction efficiency for a regular black hole. It is shown with different spin parameters (a) and different values of the regularisation parameter (l), where $l = 0$ is for the Kerr black hole. The maximum efficiency of energy extracted in the Kerr black hole at extreme spin is 20.71%, which is the well-known result for a rotating black hole, whereas for regular black holes it could be greater than that of the Kerr black hole. With increasing regularisation parameter (l), the energy extraction efficiency increases in the regular black hole, as can be seen in (Figure 2). The maximum efficiency of energy extraction in the regular black hole at extreme spin is 585.65% for $l = 1.6$. The variation between extracted energy with $l = 0$ and $l = 1.6$ is comparably minimal at slow rotation (where the spin parameter is half of the mass), whereas it is substantially larger for the high spin parameter, as shown in Figure 3. As noted previously, the ergoregion is maximum at the extreme objects' spin, resulting in the maximum energy extraction efficiency. The ergoregion reduces with decreasing spin parameters, causing the reduction of energy extraction efficiency.

Table 1. In the given table, the efficiency of energy extraction is calculated in a regular black hole spacetime for different $l(0.4, 0.8, 1.2, 1.6)$, and comparison with the Kerr black hole is given ($l = 0$).

| No. | Spin Parameter (a) | l = 0 | l = 0.4 | l = 0.8 | l = 1.2 | l = 1.6 |
|-----|--------------------|---------|---------|---------|---------|---------|
| 1 | 0.1 | 0.0627 | 0.0706 | 0.0981 | 0.1583 | 0.4558 |
| 2 | 0.2 | 0.2544 | 0.2868 | 0.4000 | 0.6480 | 1.8704 |
| 3 | 0.3 | 0.5859 | 0.6621 | 0.9295 | 1.5163 | 4.3963 |
| 4 | 0.4 | 1.0774 | 1.2226 | 1.7331 | 2.8560 | 8.3360 |
| 5 | 0.5 | 1.7638 | 2.0133 | 2.8939 | 4.8358 | 14.2433 |
| 6 | 0.6 | 2.7046 | 3.1130 | 4.5622 | 7.7680 | 23.161 |
| 7 | 0.7 | 4.0084 | 4.6698 | 7.0349 | 12.2844 | 37.2457 |
| 8 | 0.8 | 5.9017 | 7.0058 | 10.9976 | 19.887 | 61.8034 |
| 9 | 0.9 | 9.0098 | 11.0657 | 18.6299 | 35.51 | 115.227 |
| 10 | 0.93 | 10.466 | 13.0792 | 22.7707 | 44.3966 | 147.24 |
| 11 | 0.96 | 12.5 | 16.0286 | 29.2575 | 58.7556 | 201.265 |
| 12 | 0.99 | 16.1956 | 21.8635 | 43.5115 | 91.6925 | 334.925 |
| 13 | 1 | 20.7107 | 30.014 | 66.3072 | 147.02 | 585.65 |

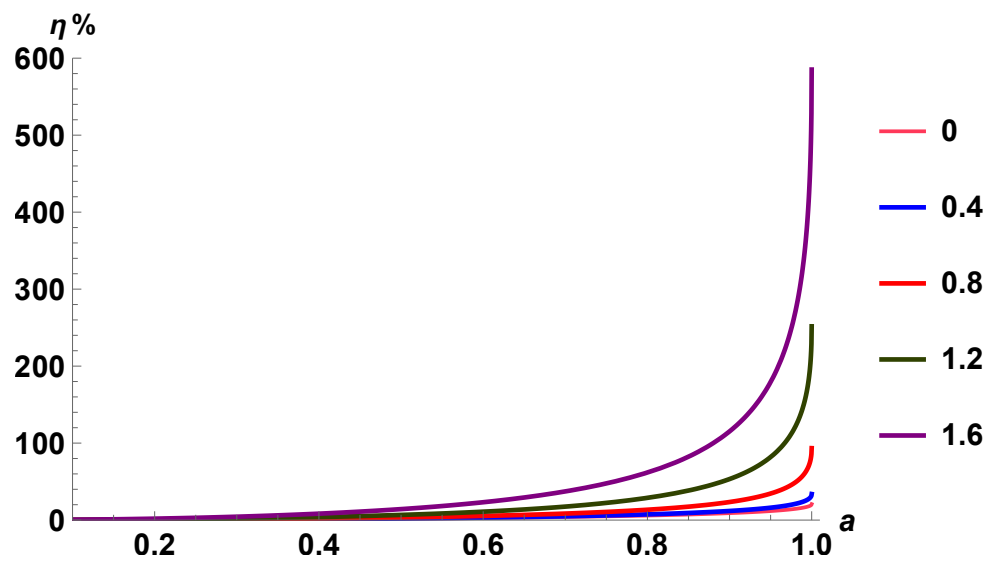


Figure 3. Extraction efficiency vs. spin parameter for a regular black hole. The bar on the right side of the page beside the figure represents the values of the regularisation parameter l , where $l = 0$ for the Kerr black hole.

4.2. A Singular Black Hole

Now consider the singular black hole solution in (14), which can be obtained from the Kerr metric after using $\nu = 3$ in the rescaling factor (15). After that, the line element for a singular black hole can be written as

$$ds_{sing}^2 = \left(1 + \frac{l^2}{\Sigma}\right)^3 \left(-\left(1 - \frac{2Mr}{\Sigma}\right)dt^2 - \frac{4Mar}{\Sigma} \sin^2\theta dt d\phi + \frac{\Sigma}{\Delta} dr^2 + \Sigma d\theta^2 + \left(a^2 + r^2 + \frac{2Mra^2 \sin^2\theta}{\Sigma}\right) \sin^2\theta d\phi^2\right), \quad (23)$$

where ‘sing’ refers to the singular black hole. The maximum efficiency that can be extracted from a singular black hole can be explored using Equation (7) with $\theta = \pi/2$:

$$\eta_{max(sing)} = \left(\frac{2a^2 M^2 (l^2 + r^2)^3}{r^7 (a^2 (2M + r) + r^3) \sqrt{1 - \frac{(l^2 + r^2)^3 (r - 2M)}{r^7}}} + \frac{\sqrt{1 - \frac{(l^2 + r^2)^3 (r - 2M)}{r^7}} + 1}{2\sqrt{1 - \frac{(l^2 + r^2)^3 (r - 2M)}{r^7}}} - 1 \right) 100. \quad (24)$$

Table 2 represents the energy extraction efficiency for a singular black hole. It is shown with different spin parameters (a) and different values of the regularisation parameter (l), where $l = 0$ is for the Kerr black hole. For a singular black hole, the efficiency of extracted energy could be greater than that of the Kerr black hole. With increasing regularisation parameter (l), the energy extraction efficiency increases in the singular black hole, as can be seen from Table 2. For $l = 1.6$, the maximum energy extracted in the singular black hole at extreme spin is 289.55%. The variation between extracted energy with $l = 0$ and $l = 1.6$ is comparably minimal at slow rotation (where the spin parameter is half of the mass), as it is substantially larger with the high spin parameter. This is also represented in Figure 4. Regular and singular black holes’ energy extraction efficiencies are significantly greater than that of the Kerr black hole. Note that a regular black hole, on the other hand, has even more extracted energy than a singular black hole.

Table 2. Efficiency of energy extraction for a singular black hole spacetime for different $l(0.4, 0.8, 1.2, 1.6)$, and comparison with the Kerr black hole ($l = 0$).

| No. | Spin Parameter (a) | $l = 0$ | $l = 0.4$ | $l = 0.8$ | $l = 1.2$ | $l = 1.6$ |
|-----|--------------------|---------|-----------|-----------|-----------|-----------|
| 1 | 0.1 | 0.0627 | 0.0734 | 0.1139 | 0.2155 | 0.2779 |
| 2 | 0.2 | 0.2544 | 0.2985 | 0.4650 | 0.8840 | 1.1396 |
| 3 | 0.3 | 0.5859 | 0.6897 | 1.0836 | 2.0767 | 2.6758 |
| 4 | 0.4 | 1.0774 | 1.2752 | 2.0292 | 3.9345 | 5.0652 |
| 5 | 0.5 | 1.7638 | 2.104 | 3.4087 | 6.7152 | 8.6324 |
| 6 | 0.6 | 2.7046 | 3.2620 | 5.4190 | 10.9033 | 13.9803 |
| 7 | 0.7 | 4.0084 | 4.9127 | 8.4550 | 17.4932 | 22.3309 |
| 8 | 0.8 | 5.9017 | 7.4153 | 13.4498 | 28.9005 | 36.6025 |
| 9 | 0.9 | 9.0098 | 11.8417 | 23.4581 | 53.3091 | 66.4615 |
| 10 | 0.93 | 10.466 | 14.0743 | 29.0711 | 67.6721 | 83.6705 |
| 11 | 0.96 | 12.5 | 17.3899 | 38.0852 | 91.5133 | 111.747 |
| 12 | 0.99 | 16.1956 | 24.1065 | 58.6912 | 148.786 | 177.178 |
| 13 | 1 | 20.7107 | 33.8248 | 93.4743 | 251.85 | 289.551 |

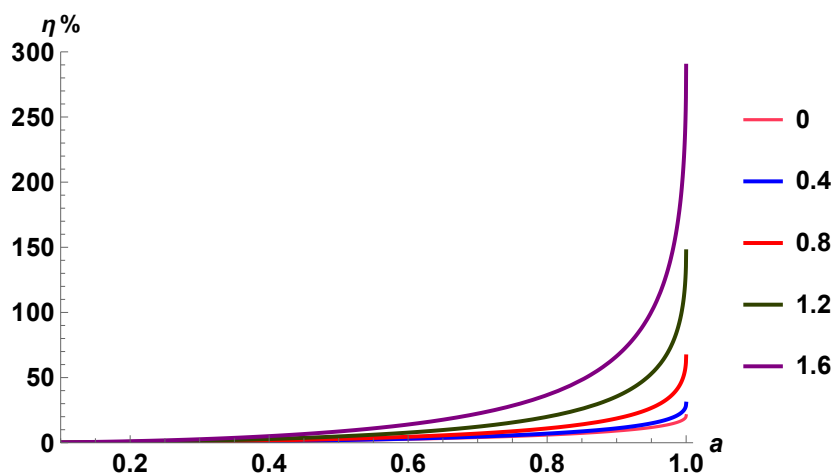


Figure 4. Energy extraction efficiency vs. spin parameter for a singular black hole. The bar on the right side of the page beside the figure represents the values of the regularisation parameter l , where $l = 0$ for the Kerr black hole.

For maximum energy extraction efficiency, we have considered that the splitting of a particle happens exactly on the event horizon. Figure 5 represents the change in the energy extraction efficiency with particle splitting or decay occurring away from the horizon.

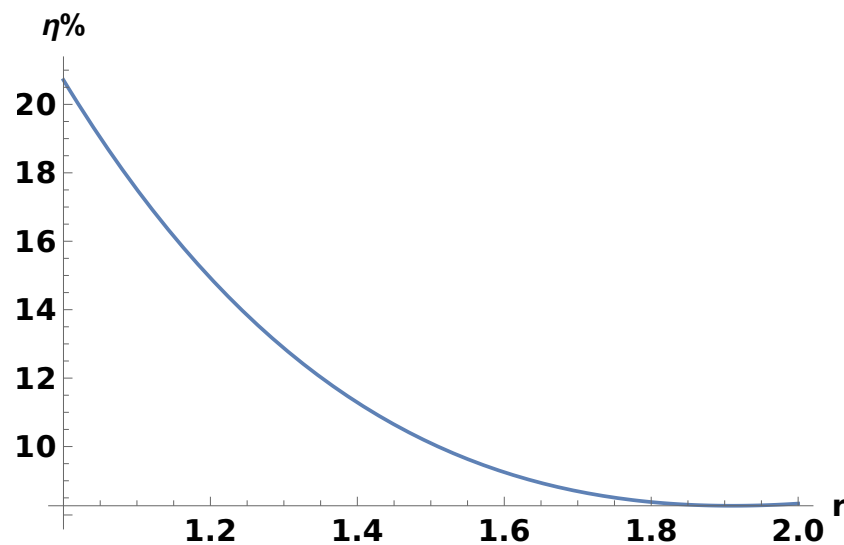


Figure 5. Change in efficiency as particle splitting or decay occurs away from the horizon. The parameters are $M = 1$, $l = 0$, and $a = 1$. The radii of the event horizon and the ergoregion are 1 and 2, respectively.

5. Discussion and Conclusions

In this paper, we conducted a comparative investigation of energy extraction using the Penrose process in rotating regular versus singular spacetimes. First, we discussed the Penrose process. Then, we examined the rotating Simpson–Visser spacetime, which has a family of different solutions, and studied how the ergoregion and horizons change as the spin and regularisation parameters change. Meanwhile, in conformal gravity, we investigated the efficiency of energy extraction in singular and regular black hole spacetime and compared it to that of a Kerr black hole. The following are the outcomes of this study.

- In Simpson–Visser spacetime, the ergoregion is dependent on the regularisation parameter (l). It is evident that the ergoregion and outer/inner horizons show significant changes as the spin parameter and regularisation parameter change. The Penrose process to extract rotational energy from rotating objects is exclusively dependent on the ergoregion, and the purpose of this study was to see how the Penrose process might be used to extract the maximum energy from a non-singular compact object such as a wormhole or a regular black hole. As the ergoregion and horizons differ from that of a Kerr black hole, the efficiency of energy extraction should be different from that of a Kerr black hole. Unexpectedly, we found that the energy extraction in rotating Simpson–Visser spacetime is the same as in a Kerr black hole. This is because the efficiency of energy extraction (η_{max}) is independent of the regularisation parameter l . The study in [102] gives a similar type of conclusion that the size of the ergoregion seems to play no role in energy extraction using the Penrose process.
- The possible reason behind this is that in the rotating Simpson–Visser case, the energy extraction efficiency remains unchanged as we change the regularisation parameter, and thus the corresponding event horizon radius, Cauchy horizon radius, and ergo-radius change. Now, we have considered the Penrose process taking place just at the event horizon. Hence, changing the regularisation parameter does not change the scenario of the process, as the phenomena still occur at the event horizons of two corresponding different regular black hole structures. In that case, since we have considered similar values of spin parameter a , the frame-dragging rates of spacetime geometries with corresponding values of the regularisation parameter will be the same. Now, as the Penrose process mainly depends on the frame-dragging effect of the spacetime, at the event horizon, the efficiency will always be maximum. In that case, for any given rotating Simpson–Visser black hole, for different regularisation

parameters, and thus for corresponding different event horizon radii, the energy extraction efficiency remains the same.

- However, one can consider the case in which for specific values of event horizon radius, Cauchy horizon radius, and ergo-radius, the Penrose process takes place at a different radial distance r . In such a case, as the radial distance increases from event horizon radius r_{eh} to outer ergoradius r_{erg} , the efficiency gradually decreases. This is because as we move away from the horizon, the frame-dragging effect of spacetime structure and thus the angular velocity decreases.
- Using the conformal transformation classically, one can resolve the spacetime singularity problem that arises in Einstein's general theory of relativity. The singular and regular black holes considered here are the solutions of CEFE derived in [97]. Depending on the parameter ν , one gets the spacetime solution with or without singularity. The expressions of ergoregions in singular and regular black hole spacetimes are independent of the regularisation parameter (l). Thus, the ergoregions for regular and singular black holes are similar to that of the Kerr black hole. As explained earlier, the ergoregions and horizons show significantly evident changes for the cases $a > M$ and $a < M$. However, we consider only the case in which $a < M$ for which the horizons exist.
- It is evident from this investigation that the efficiency of energy extraction varies as the size of the ergoregion changes. Interestingly, even though the ergoregions in regular and singular black holes are similar to those in the Kerr black hole, the efficiency for energy extraction is significantly larger in regular and singular black holes. In a CEFE solution, the efficiency of energy extraction is large enough in a regular black hole rather than in a singular black hole case. However, one may notice from Figures 3 and 4 that in all compact objects, the energy extraction is nearly the same for spin parameters up to 0.5. The maximum difference in energy extraction efficiency occurs at the extreme spin parameter ($a = M$).
- Here, the energy extraction efficiency with the conformal transformation is more than 100%, which means that after the Penrose process when a particle escapes the ergoregion, it has energy higher than its initial energy when the particle entered in the negative energy orbit region. The energy extraction efficiency of 100% was first shown in 1985 [103,104]. Additionally, based on the conformal geometry in [105], it has been shown that the energy extraction efficiency from a Kerr naked singularity can reach 157% using the magnetic Penrose process.
- In this work, the phenomenology of energy extraction for a neutral test particle is explained for singular and regular black holes. One may study the efficiency of energy extraction in the presence of a magnetic field or for charged test particles.

Author Contributions: Conceptualization, P.B., P.S.J., V.P. and K.A.; methodology, V.P. and K.A.; validation, P.B. and P.S.J.; formal analysis, P.B.; investigation, V.P., K.A., P.B. and P.S.J.; writing—original draft preparation, V.P., K.A. and P.B.; writing—review and editing, P.B. and P.S.J.; visualization, P.S.J.; supervision, P.S.J. All authors have read and agreed to the published version of the manuscript.

Funding: This research received no external funding.

Acknowledgments: The authors would like to thank the anonymous referees for their valuable suggestions. The authors would like to express their gratitude towards Divyesh Solanki, Siddharth Madan, Saurabh, and Ashwathi Nair for all their valuable suggestions and astute insights. V.P. would like to acknowledge the support of the SHODH fellowship (ScHeme Of Developing High quality research—MYSY).

Data Availability Statement: No data were used to support this study.

Conflicts of Interest: The authors declare no conflict of interest.

References

1. Akiyama, K. et al. [Event Horizon Telescope] First Sagittarius A* Event Horizon Telescope Results. I. The Shadow of the Supermassive Black Hole in the Center of the Milky Way. *Astrophys. J. Lett.* **2022**, *930*, L12. [[CrossRef](#)]
2. Broderick, A.E. et al. [Event Horizon Telescope] Characterizing and Mitigating Intraday Variability: Reconstructing Source Structure in Accreting Black Holes with mm-VLBI. *Astrophys. J. Lett.* **2022**, *930*, L21. [[CrossRef](#)]
3. Wielgus, M. et al. [Event Horizon Telescope] Millimeter Light Curves of Sagittarius A* Observed during the 2017 Event Horizon Telescope Campaign. *Astrophys. J. Lett.* **2022**, *930*, L19. [[CrossRef](#)]
4. Akiyama, K. et al. [Event Horizon Telescope] First Sagittarius A* Event Horizon Telescope Results. II. EHT and Multiwavelength Observations, Data Processing, and Calibration. *Astrophys. J. Lett.* **2022**, *930*, L13. [[CrossRef](#)]
5. Akiyama, K. et al. [Event Horizon Telescope] First Sagittarius A* Event Horizon Telescope Results. III. Imaging of the Galactic Center Supermassive Black Hole. *Astrophys. J. Lett.* **2022**, *930*, L14. [[CrossRef](#)]
6. Akiyama, K. et al. [Event Horizon Telescope] First Sagittarius A* Event Horizon Telescope Results. V. Testing Astrophysical Models of the Galactic Center Black Hole. *Astrophys. J. Lett.* **2022**, *930*, L16. [[CrossRef](#)]
7. Akiyama, K. et al. [Event Horizon Telescope] First Sagittarius A* Event Horizon Telescope Results. VI. Testing the Black Hole Metric. *Astrophys. J. Lett.* **2022**, *930*, L17. [[CrossRef](#)]
8. Farah, J. et al. [Event Horizon Telescope] Selective Dynamical Imaging of Interferometric Data. *Astrophys. J. Lett.* **2022**, *930*, L18. [[CrossRef](#)]
9. Gralla, S.E.; Holz, D.E.; Wald, R.M. Black hole shadows, photon rings, and lensing rings. *Phys. Rev. D* **2019**, *100*, 024018. [[CrossRef](#)]
10. Abdikamalov, A.B.; Abdujabbarov, A.A.; Ayzenberg, D.; Malafarina, D.; Bambi, C.; Ahmedov, B. Black hole mimicker hiding in the shadow: Optical properties of the γ metric. *Phys. Rev. D* **2019**, *100*, 024014. [[CrossRef](#)]
11. Dey, D.; Bhattacharya, K.; Sarkar, T. Astrophysics of Bertrand space-times. *Phys. Rev. D* **2013**, *88*, 083532. [[CrossRef](#)]
12. Dey, D.; Shaikh, R.; Joshi, P.S. Perihelion precession and shadows near black holes and naked singularities. *Phys. Rev. D* **2020**, *102*, 044042. [[CrossRef](#)]
13. Ohgami, T.; Sakai, N. Wormhole shadows. *Phys. Rev. D* **2015**, *91*, 124020. [[CrossRef](#)]
14. Sakai, N.; Saida, H.; Tamaki, T. Gravastar shadows. *Phys. Rev. D* **2014**, *90*, 104013. [[CrossRef](#)]
15. Bambhaniya, P.; Joshi, P.S. Probing the Shadow Image of the Sagittarius A* with Event Horizon Telescope. *arXiv* **2022**, arXiv:2202.00588.
16. Solanki, D.N.; Bambhaniya, P.; Dey, D.; Joshi, P.S.; Pathak, K.N. Shadows and precession of orbits in rotating Janis–Newman–Winicour spacetime. *Eur. Phys. J. C* **2022**, *82*, 1–13. [[CrossRef](#)]
17. Bambhaniya, P.; Dey, D.; Joshi, A.B.; Joshi, P.S.; Solanki, D.N.; Mehta, A. Shadows and negative precession in non-Kerr spacetime. *Phys. Rev. D* **2021**, *103*, 084005. [[CrossRef](#)]
18. Bambi, C. Testing black hole candidates with electromagnetic radiation. *Rev. Mod. Phys.* **2017**, *89*, 025001. [[CrossRef](#)]
19. Shaikh, R. Shadows of rotating wormholes. *Phys. Rev. D* **2018**, *98*, 024044. [[CrossRef](#)]
20. Jusufi, K.; Saurabh, S. Black hole shadows in Verlinde’s emergent gravity. *Mon. Not. R. Astron. Soc.* **2021**, *503*, 1310–1318. [[CrossRef](#)]
21. Lee, B.-H.; Lee, W.; Myung, Y.S. Shadow cast by a rotating black hole with anisotropic matter. *Phys. Rev. D* **2021**, *103*, 064026. [[CrossRef](#)]
22. Shaikh, R.; Banerjee, P.; Paul, S.; Sarkar, T. Strong gravitational lensing by wormholes. *J. Cosmol. Astropart. Phys.* **2019**, *2019*, 28. [[CrossRef](#)]
23. Shaikh, R.; Banerjee, P.; Paul, S.; Sarkar, T. A novel gravitational lensing feature by wormholes. *Phys. Lett. B* **2018**, *789*, 270–275. [[CrossRef](#)]
24. Paul, S. Strong gravitational lensing by a strongly naked null singularity. *Phys. Rev. D* **2020**, *102*, 064045. [[CrossRef](#)]
25. Virbhadra, K.S.; Keeton, C.R. Time delay and magnification centroid due to gravitational lensing by black holes and naked singularities. *Phys. Rev. D* **2008**, *77*, 124014. [[CrossRef](#)]
26. Gyulchev, G.N.; Yazadjiev, S.S. Gravitational lensing by rotating naked singularities. *Phys. Rev. D* **2008**, *78*, 083004. [[CrossRef](#)]
27. Kala, S.; Saurabh; Nandan, H.; Sharma, P. Deflection of light and shadow cast by a dual-charged stringy black hole. *Int. J. Mod. Phys. A* **2020**, *35*, 2050177. [[CrossRef](#)]
28. Sahu, S.; Patil, M.; Narasimha, D.; Joshi, P.S. Can strong gravitational lensing distinguish naked singularities from black holes? *Phys. Rev. D* **2012**, *86*, 063010. [[CrossRef](#)]
29. Liu, C.; Zhu, T.; Wu, Q. Thin accretion disk around a four-dimensional Einstein-Gauss-Bonnet black hole *. *Chin. Phys. C* **2021**, *45*, 015105. [[CrossRef](#)]
30. Joshi, P.S.; Malafarina, D.; Narayan, R. Distinguishing black holes from naked singularities through their accretion disc properties. *Class. Quantum Gravity* **2013**, *31*, 015002. [[CrossRef](#)]
31. Bambhaniya, P.; Saurabh; Jusufi, K.; Joshi, P.S. Thin accretion disk in the Simpson-Visser black-bounce and wormhole spacetimes. *Phys. Rev. D* **2022**, *105*, 023021. [[CrossRef](#)]
32. Rahaman, F.; Manna, T.; Shaikh, R.; Aktar, S.; Mondal, M.; Samanta, B. Thin accretion disks around traversable wormholes. *Nucl. Phys. B* **2021**, 972. [[CrossRef](#)]
33. Harko, T.; Kovacs, Z.; Lobo, F.S.N. Can accretion disk properties distinguish gravastars from black holes? *Class. Quantum Gravity* **2009**, *26*, 215006. [[CrossRef](#)]

34. Tahelyani, D.; Joshi, A.B.; Dey, D.; Joshi, P.S. Comparing thin accretion disk properties of naked singularities and black holes. *arXiv* **2022**, arXiv:2205.04055.
35. Guo, J.-Q.; Joshi, P.S.; Narayan, R.; Zhang, L. Accretion disks around naked singularities. *Class. Quantum Gravity* **2020**, *38*, 035012. [[CrossRef](#)]
36. Chowdhury, A.N.; Patil, M.; Malafarina, D.; Joshi, P.S. Circular geodesics and accretion disks in the Janis-Newman-Winicour and gamma metric spacetimes. *Phys. Rev. D* **2012**, *85*, 104031. [[CrossRef](#)]
37. Martínez, C.; Parra, N.; Valdés, N.; Zanelli, J. Geodesic structure of naked singularities in AdS3 spacetime. *Phys. Rev. D* **2019**, *100*, 024026. [[CrossRef](#)]
38. Madan, S.; Bambhaniya, P. Tidal force effects and periodic orbits in null naked singularity spacetime. *arXiv* **2022**, arXiv:2201.13163.
39. Hackmann, E.; Kagramanova, V.; Kunz, J.; Lämmerzahl, C. Analytic solutions of the geodesic equation in axially symmetric space-times. *Eur. Lett.* **2009**, *88*, 30008. [[CrossRef](#)]
40. Hackmann, E.; Lämmerzahl, C.; Obukhov, Y.N.; Puetzfeld, D.; Schaffer, I. Motion of spinning test bodies in Kerr spacetime. *Phys. Rev. D* **2014**, *90*, 064035. [[CrossRef](#)]
41. Potashov, I.M.; Tchamarina, J.; Tsirulev, A.N. Bound orbits near scalar field naked singularities. *Eur. Phys. J. C* **2019**, *79*, 709. [[CrossRef](#)]
42. Joshi, A.B.; Bambhaniya, P.; Dey, D.; Joshi, P.S. Timelike geodesics in naked singularity and black hole spacetimes II. *arXiv* **2019**, arXiv:1909.08873.
43. Bambhaniya, P.; Joshi, A.B.; Dey, D.; Joshi, P.S. Timelike geodesics in naked singularity and black hole spacetimes. *Phys. Rev. D* **2019**, *100*, 124020. [[CrossRef](#)]
44. Dey, D.; Joshi, P.S.; Joshi, A.; Bambhaniya, P. Towards an observational test of black hole versus naked singularity at the galactic center. *Int. J. Mod. Phys. D* **2019**, *28*, 1930024. [[CrossRef](#)]
45. Bambhaniya, P.; Solanki, D.N.; Dey, D.; Joshi, A.B.; Joshi, P.S.; Patel, V. Precession of timelike bound orbits in Kerr spacetime. *Eur. Phys. J.* **2021**, *81*, 1–11. [[CrossRef](#)]
46. Guo, S.; Li, G.R.; Li, G.P. Shadow thermodynamics of AdS black hole in regular spacetime. *arXiv* **2022**, arXiv:2205.04957.
47. Kala, S.; Nandan, H.; Sharma, P. Shadow and weak gravitational lensing of a rotating regular black hole in a non-minimally coupled Einstein-Yang-Mills theory in the presence of plasma. *Eur. Phys. J. Plus* **2022**, *137*, 1–18. [[CrossRef](#)]
48. Ahmed, F.; Singh, D.V.; Ghosh, S.G. Five dimensional rotating regular black holes and shadow. *Gen. Relativ. Gravit.* **2022**, *54*, 1–22. [[CrossRef](#)]
49. Jafarzade, K.; Zangeneh, M.K.; Lobo, F.S. Observational optical constraints of regular black holes. *arXiv* **2022**, arXiv:2106.13893.
50. Qin, X.; Chen, S.; Jing, J. Image of a regular phantom compact object and its luminosity under spherical accretions. *Class. Quantum Gravity* **2021**, *38*, 115008. [[CrossRef](#)]
51. Mondal, M.; Yadav, A.K.; Pradhan, P.; Islam, S.; Rahaman, F. Null geodesics and QNMs in the field of regular black holes. *Int. J. Mod. Phys. D* **2021**, *30*, 2150095. [[CrossRef](#)]
52. Ghosh, S.G.; Amir, M.; Maharaj, S.D. Ergosphere and shadow of a rotating regular black hole. *Nucl. Phys. B* **2020**, *957*, 115088. [[CrossRef](#)]
53. Kumar, R.; Ghosh, S.G. Photon ring structure of rotating regular black holes and no-horizon spacetimes. *Class. Quantum Gravity* **2021**, *38*, 085010. [[CrossRef](#)]
54. Li, Z.; Bambi, C. Measuring the Kerr spin parameter of regular black holes from their shadow. *J. Cosmol. Astropart. Phys.* **2014**, *2014*, 041. [[CrossRef](#)]
55. Narzilloev, B.; Rayimbaev, J.; Shaymatov, S.; Abdujabbarov, A.; Ahmedov, B.; Bambi, C. Dynamics of test particles around a Bardeen black hole surrounded by perfect fluid dark matter. *Phys. Rev. D* **2020**, *102*, 104062. [[CrossRef](#)]
56. Benavides-Gallego, C.A.; Abdujabbarov, A.; Malafarina, D.; Ahmedov, B.; Bambi, C. Charged particle motion and electromagnetic field in γ spacetime. *Phys. Rev. D* **2019**, *99*, 044012. [[CrossRef](#)]
57. Fathi, M.; Olivares, M.; Villanueva, J. Ergosphere, Photon Region Structure, and the Shadow of a Rotating Charged Weyl Black Hole. *Galaxies* **2021**, *9*, 43. [[CrossRef](#)]
58. Abramowicz, M.A.; Calvani, M.; Nobili, L. Runaway instability in accretion disks orbiting black holes. *Nature* **1983**, *302*, 597–599. [[CrossRef](#)]
59. Rees, M.J.; Begelman, M.C.; Blandford, R.D.; Phinney, S. Ion-supported tori and the origin of radio jets. *Nature* **1982**, *295*, 17–21. [[CrossRef](#)]
60. Penrose, R.; Floyd, R.M. Extraction of Rotational Energy from a Black Hole. *Nat. Phys. Sci.* **1971**, *229*, 177–179. [[CrossRef](#)]
61. Wheeler, J. Study Week on Nuclei of Galaxies, ed DJK O’Connell. *North Holl. Pontif. Acad. Scr. Varia* **1971**, *35*, 539.
62. Ghosh, S.G.; Sheoran, P. Higher dimensional non-Kerr black hole and energy extraction. *Phys. Rev. D* **2014**, *89*, 024023. [[CrossRef](#)]
63. Liu, C.; Chen, S.; Jing, J. ROTATING NON-KERR BLACK HOLE AND ENERGY EXTRACTION. *Astrophys. J. Lett.* **2012**, *751*, 148. [[CrossRef](#)]
64. Nozawa, M.; Maeda, K.-I. Energy extraction from higher dimensional black holes and black rings. *Phys. Rev. D* **2005**, *71*, 084028. [[CrossRef](#)]
65. Wagh, S.M.; Dadhich, N. The energetics of black holes in electromagnetic fields by the penrose process. *Phys. Rep.* **1989**, *183*, 137–192. [[CrossRef](#)]

66. Zaslavskii, O.B. High-energy collision of particles in the magnetic field far from black holes. *Mod. Phys. Lett. A* **2014**, *29*, 1450151. [[CrossRef](#)]
67. Zaslavskii, O.B. Energy extraction from extremal charged black holes due to the Banados-Silk-West effect. *Phys. Rev. D* **2012**, *86*, 124039. [[CrossRef](#)]
68. Tsukamoto, N.; Bambi, C. Collisional Penrose process in a rotating wormhole spacetime. *Phys. Rev. D* **2015**, *91*, 104040. [[CrossRef](#)]
69. Zaslavskii, O.B. Super-Penrose process with charged particles near naked singularity. *arXiv* **2022**, arXiv:2204.03314.
70. Zaslavskii, O.B. Super-Penrose process for extremal charged white holes. *Mod. Phys. Lett. A* **2020**, *36*, 2150020. [[CrossRef](#)]
71. Gupta, K.; Law, Y.T.A.; Levin, J. Penrose process for a charged black hole in a uniform magnetic field. *Phys. Rev. D* **2021**, *104*, 084059. [[CrossRef](#)]
72. Zaslavskii, O.B. Super-Penrose process for extremal rotating neutral white holes. *Gen. Relativ. Gravit.* **2020**, *52*, 1–11. [[CrossRef](#)]
73. Zaslavskii, O.B. Center of mass energy of colliding electrically neutral particles and super-Penrose process. *Phys. Rev. D* **2019**, *100*, 024050. [[CrossRef](#)]
74. Hejda, F.; Lemos, J.P.S.; Zaslavskii, O.B. Extraction of energy from an extremal rotating electrovacuum black hole: Particle collisions in the equatorial plane. *Phys. Rev. D* **2022**, *105*, 024014. [[CrossRef](#)]
75. Hejda, F.; Bičák, J.; Zaslavskii, O.B. Extraction of energy from an extremal rotating electrovacuum black hole: Particle collisions along the axis of symmetry. *Phys. Rev. D* **2019**, *100*, 064041. [[CrossRef](#)]
76. Zaslavskii, O.B. New Scenarios of High-Energy Particle Collisions Near Wormholes. *Universe* **2020**, *6*, 227. [[CrossRef](#)]
77. Pavlov, Y.V.; Zaslavskii, O.B. Kinematic Censorship as a Constraint on Allowed Scenarios of High-Energy Particle Collisions. *Gravit. Cosmol.* **2019**, *25*, 390–396. [[CrossRef](#)]
78. Zaslavskii, O.B. Maximum efficiency of the collisional Penrose process. *Phys. Rev. D* **2016**, *94*, 064048. [[CrossRef](#)]
79. Zaslavskii, O.B. Rotation as an origin of high energy particle collisions. *Mod. Phys. Lett. A* **2016**, *31*, 1650029. [[CrossRef](#)]
80. Shaymatov, S.; Sheoran, P.; Becerril, R.; Nucamendi, U.; Ahmedov, B. Efficiency of Penrose process in spacetime of axially symmetric magnetized Reissner-Nordström black hole. *arXiv* **2022**, arXiv:2204.02026
81. Gibbons, G.W.; Horowitz, G.T.; Townsend, P.K. Higher-dimensional resolution of dilatonic black-hole singularities. *Class. Quantum Gravity* **1995**, *12*, 297–317. [[CrossRef](#)]
82. Lawrence, A.; Martinec, E. String field theory in curved spacetime and the resolution of spacelike singularities. *Class. Quantum Gravity* **1996**, *13*, 63–95. [[CrossRef](#)]
83. Easson, D.A. Towards a stringy resolution of the cosmological singularity. *Phys. Rev. D* **2003**, *68*, 043514. [[CrossRef](#)]
84. Husain, V.; Winkler, O. Quantum resolution of black hole singularities. *Class. Quantum Gravity* **2005**, *22*, L127–L133. [[CrossRef](#)]
85. De Roo, F. Geometrical Resolution of Spacetime Singularities. Ph.D. Thesis, Vrije Universiteit Brussel, Brussel, Belgium, 2010.
86. Cheng-Zhou, L.; Guo-Xiang, Y.; Zhi-Kun, X. The spacetime singularity resolution of Schwarzschild-de Sitter black hole in loop quantum gravity. *Acta Phys. Sin.* **2010**, *59*, 1487–1493. [[CrossRef](#)]
87. Philipp, H.v.L. Resolution of Curvature Singularities in Black Holes and the Early Universe. 2010. Available online: <https://edoc.uni-muenchen.de/11865/> (accessed on 8 September 2022).
88. Singh, P. Bianchi-I spacetimes in loop quantum cosmology: Physics of singularity resolution. *J. Phys. Conf. Ser.* **2012**, *360*, 012008. [[CrossRef](#)]
89. Corichi, A.; Karami, A.; Montoya, E. Loop Quantum Cosmology: Anisotropy and Singularity Resolution. In *Relativity and Gravitation*; Springer: Cham, Switzerland, 2014; pp. 469–477. [[CrossRef](#)]
90. Lee, S.; Roychowdhury, R.; Yang, H.S. Topology change of spacetime and resolution of spacetime singularity in emergent gravity. *Phys. Rev. D* **2013**, *87*, 126002. [[CrossRef](#)]
91. Kreienbuehl, A.; Pawłowski, T. Singularity resolution from polymer quantum matter. *Phys. Rev. D* **2013**, *88*, 043504. [[CrossRef](#)]
92. Blanchette, K.; Das, S.; Hergott, S.; Rastgoo, S. Black hole singularity resolution via the modified Raychaudhuri equation in loop quantum gravity. *Phys. Rev. D* **2021**, *103*, 084038. [[CrossRef](#)]
93. Mosani, K.; Dey, D.; Bhattacharya, K.; Joshi, P.S. Singularity resolution in gravitational collapse. *Phys. Rev. D* **2022**, *105*, 064048. [[CrossRef](#)]
94. Shaikh, R.; Pal, K.; Sarkar, T. Constraining alternatives to the Kerr black hole. *Mon. Not. R. Astron. Soc.* **2021**, *506*, 1229–1236. [[CrossRef](#)]
95. Mazza, J.; Franzin, E.; Liberati, S. A novel family of rotating black hole mimickers. *J. Cosmol. Astropart. Phys.* **2021**, *2021*, 082. [[CrossRef](#)]
96. Bronnikov, K.A.; Walia, R.K. Field sources for Simpson-Visser spacetimes. *Phys. Rev. D* **2022**, *105*, 044039. [[CrossRef](#)]
97. Bambi, C.; Modesto, L.; Rachwal, L. Spacetime completeness of non-singular black holes in conformal gravity. *J. Cosmol. Astropart. Phys.* **2017**, *2017*, 003. [[CrossRef](#)]
98. Zhang, Q.; Modesto, L.; Bambi, C. A general study of regular and singular black hole solutions in Einstein's conformal gravity. *Eur. Phys. J. C* **2018**, *78*, 506. [[CrossRef](#)]
99. Glass, E.N.; Krisch, J.P. Spinning up asymptotically flat spacetimes. *Class. Quantum Gravity* **2004**, *21*, 5543–5553. [[CrossRef](#)]
100. Simpson, A.; Visser, M. Black-bounce to traversable wormhole. *J. Cosmol. Astropart. Phys.* **2019**, *2019*, 042. [[CrossRef](#)]
101. Islam, S.U.; Kumar, J.; Ghosh, S.G. Strong gravitational lensing by rotating Simpson-Visser black holes. *J. Cosmol. Astropart. Phys.* **2021**, *2021*, 13. [[CrossRef](#)]

102. Franzin, E.; Liberati, S.; Mazza, J.; Dey, R.; Chakraborty, S. Scalar perturbations around rotating regular black holes and wormholes: Quasinormal modes, ergoregion instability, and superradiance. *Phys. Rev. D* **2022**, *105*, 124051. [[CrossRef](#)]
103. Wagh, S.M.; Dhurandhar, S.V.; Dadhich, N. Revival of the Penrose process for astrophysical applications. *Astrophys. J. Lett.* **1985**, *290*, 12–14. [[CrossRef](#)]
104. Tursunov, A.; Dadhich, N. Fifty Years of Energy Extraction from Rotating Black Hole: Revisiting Magnetic Penrose Process. *Universe* **2019**, *5*, 125. [[CrossRef](#)]
105. Stuchlik, Z. Bulletin of the Astronomical Institute of Czechoslovakia. 1980; Volume 31, p. 129. Available online: <https://ui.adsabs.harvard.edu/abs/1980BAICz..31..129S/abstract> (accessed on 8 September 2022).